Effect of anodizing on high cycle fatigue behaviour of cast AlSi8Mg-T6 alloy

Pavesi A.;Bandiera M.;Mancini A.;Tsyupa B.;Bonfanti A.;Casari D.;Barella S.;D'Errico F.;Bertasi F.

Effect of Anodizing on High Cycle Fatigue Behaviour of Cast AlSi8Mg-T6 Alloy

Arianna Pavesi[a,b], Marco Bandiera[a], Alessandro Mancini[a], Bozhena Tsyupa[a], Andrea Bonfanti[a]

Daniele Casari[c], Silvia Barella[b], Fabrizio D'Errico[b] and Federico Bertasi[a,*]

[a] R&D GCF, Brembo S.p.A. Viale Europa 2, 24040 Stezzano, Italy.

[b] Politecnico di Milano, Dipartimento di Meccanica, Via La Masa 1, 20156 Milano, Italy.

[c] Industrial Operations GCF, Aluminium Foundry, Via G. M. Scotti 66, 24030, Mapello, Italy.

*Corresponding author. *E-mail address:* federico_bertasi@brembo.it

Abstract

The work investigates the effect of anodizing on the high cycle fatigue behaviour of a high-quality cast Aluminium (AlSi8Mg-T6) alloy. Tensile and fatigue tests are carried out on both non-anodized and anodized specimens in order to highlight the differences in tensile and fatigue responses. In addition, roughness measurements, fracture surfaces analyses, metallography, instrumented micro-indentation and scanning electron microscope (SEM) inspections are performed in order to investigate the interplay between the presence of an anodic layer and the fatigue life of anodized specimens.

It is demonstrated that, after anodizing, AlSi8Mg-T6 specimens shows a worsening of the fatigue performance at medium-low stress amplitudes (130 and 110MPa). In addition, fracture surface analysis reveals that the presence of the anodic layer modifies the fatigue crack initiation and early growth mechanisms. The manuscript paves the way for an accurate fatigue design of anodized, cast AlSix components.

Keywords: Aluminium alloys, Anodizing, High cycle fatigue, Fatigue crack initiation, Surface roughness.

1. Introduction

Cast Aluminium-Silicon (AlSix) alloys are key materials for automotive and aerospace industries due to their: a) low density; b) excellent mechanical performances; and c) superior castability [1,2]. Nevertheless, corrosion and wear resistance of AlSix are often lacking and conversion/coating strategies need to be applied [1,3]. In this context, anodizing is one of the most common conversion methods which is use to increase both the corrosion and wear resistance of the Al-based materials [3,4].

At a deeper level, anodizing is an electrochemical process that allows the controlled growth of a thick amorphous Al_2O_3 layer on the surface of an Aluminium component. The anodizing process includes at least the following steps [4]: 1) acidic and/or alkaline pre-treatments; 2) electrochemical anodizing process while the part is immersed in a suitable electrolyte; and 3) post-treatments.

It is clear that different coating features (e.g., thickness, wettability, colour, porosity, hardness, etc.) can be obtained by tuning several process parameters (e.g., pre-treatments, chemical nature of the electrolyte, current/voltage, process temperature, etc.) [4-8].

The typical microstructure of the so-obtained anodic layer is characterized by two regions: 1) a compact nanometric layer at the interface with the base metal (barrier layer); and 2) a micrometric nano-porous coating between the barrier layer and the environment [5,6]. In order to further increase the corrosion resistance of the coating, a typical post-treatment involves the sealing of the nanoporous anodic layer with different salts by means of a hydrothermal process [4,7].

In the last decades, a large variety of anodizing and sealing processes have been developed on the basis of different electrolytes (H_2SO_4, oxalate, neutral, etc.) and sealing agents (NiF_2, $K_2Cr_2O_7$, boiling water, Nickel Acetate, etc.) thus obtaining functional coatings with optimized morphological, tribological and aesthetic features [3-7].

It appears clear that the anodizing process can induce surface modifications, which could also strongly impact the fatigue life of the component. As an example, anodizing can: a) increases the surface roughness of the piece [9,10]; and b) generate internal tensile stresses and micro-voids (especially in the case of high-alloyed Aluminium alloys, e.g. cast AlSix alloys) [10-17]). These events can be

associated with the growth of an anodic layer which: a) has dissimilar mechanical properties (e.g. hardness, elastic modulus) with respect to the underneath Al matrix [11,17-19]; and b) has a brittle nature [13,18,20]. In addition, acidic or alkaline pre-treatments could lead to corrosion events on the surface of the part to be anodized due to micro-galvanic coupling phenomena between Cu or Fe - based precipitates, which are cathodic with respect to the Aluminium matrix [16,17,20,21].

Taken altogether, the careful investigation of the interplay between anodizing process and fatigue life of cast AlSix alloys becomes crucial since several anodized cast AlSix parts [22,23] can undergo fatigue stresses during their service life (e.g. automotive and aerospace components). Unlike wrought alloys [11-13,16,18,20,21, 24-29], this aspect is barely investigated in the literature for cast AlSix materials and results are not always conclusive [30,31]. On one hand, Rateick et al. [30] report that the effect of a 51μm-thick oxide layer obtained by hard anodizing on a cast AlSi5Cu1Mg alloys is negligible. On the other hand, in a recent work, Nakamura et al. [31] demonstrate that the presence of an anodic layer with a thickness equal to 10μm on a cast AlSi10Cu4Mg alloy negatively affect the fatigue strength as obtained by rotating bending fatigue tests. This discrepancy in the conclusions could be associated with different levels of casting defects, which are known to play a pivotal role in modulating the fatigue life of the cast component and are likely to overshadow the effect of the anodizing process [30,32,33].

At this regard, in this work, particular attention has been devoted to obtaining high quality casting specimens by carefully tuning several process parameters including for example: a) degassing; b) molten Aluminium temperature; c) mould temperature and design; and d) deslagging; with the aim of minimizing the effect of casting defects and maximizing that of the surface anodic layer on fatigue life.

In this scenario the manuscript investigates the effect of the anodizing process on the fatigue life of a cast AlSix alloy subjected to a technically sound melt treatment followed by a well-designed and controlled pouring practice in order to minimise casting defects. Firstly, the microstructure and the composition of the cast AlSix alloy is examined using metallographic and X-ray fluorescence

techniques in order to assess the quality of the casting process. Secondly, round cross-sectioned AlSix samples are anodized, using an optimized procedure [34]. Thirdly, non-anodized and anodized specimens are characterized in terms of: a) roughness of the surfaces; b) tensile and high cycle fatigue (HCF) tests; and c) fracture surfaces analysis. Finally, the manuscript elucidates the effect of the anodic layer on the crack nucleation mechanism and discusses the effect of anodizing on the fatigue behaviour of the alloy.

2. Experimental methods

2.1. Alloy casting and composition

Tensile and fatigue specimens are cast using a permanent-mould gravity casting machine. The alloy (total weight about 100 kg) is cast in a single batch in order to ensure that all the obtained specimens (both non-anodized and anodized) undergo an identical casting process. Particular attention is devoted to the implementation of proper foundry practices including: 1) degassing and deslagging of the alloy; 2) accurate control of molten Aluminium and mould temperatures; and 3) mould design optimisation. Raw specimens are then homogenized at 530±5°C for 7h and artificially aged at 155±5°C for 2.5h (T6 heat treatment) [35]. After T6, raw specimens are machined in shape of round cross-section specimens with standard dimensions and a mean surface roughness (R_a) less than 0.2μm, as per ISO 1099:2017 and ISO 6892-1:2019 [36,37]. After machining, half specimens undergo an anodizing process, as described in Paragraph 2.2 thus obtaining two sets of specimens namely: anodized and non-anodized. Non-anodized tensile and HCF specimens are labelled Px with 1≤x≤5 and Ey with 1≤y≤18, respectively. On the other hand, anodized tensile and HCF specimens are identified as Ax with 1≤x≤5 and as Fy with 1≤y≤18, respectively.

The chemical composition of each anodized HCF specimen is assessed by means of micro X-ray fluorescence (μ-XRF) analysis using a Bruker M4 Tornado spectrometer equipped with an Rh source. Instrumental parameters are: 50kV, 200μA, 4×4mm^2 surface, 25μm spatial resolution, 5 measurement integrations. For sake of brevity, the alloy is labelled as AlSi8Mg-T6, along the manuscript.

2.2. Anodizing

In order to investigate the effect of the anodizing process on mechanical properties of AlSi8Mg-T6, tensile and HCF specimens are anodized using a three steps procedure as follows [34,38]. Firstly, samples are: a) cleaned using a commercial detergent; and b) pre-treated in a 0.5M NaOH aqueous solution at 50±10°C for 3min. Secondly, anodizing is performed using a Biologic VMP-300 potentiostat/galvanostatat in a two-electrode configuration where the Aluminium acts as working electrode (WE) and graphite rods as counter electrodes (CEs). Optimized anodizing parameters for AlSi8Mg-T6 alloy are applied during the treatment [34]. In particular, a current density of $1.2A \cdot dm^{-2}$ is used, obtaining coatings with an average thickness equal to 15μm. A $200g \cdot L^{-1}$ H_2SO_4 aqueous stirred solution at 17.0±0.1°C is used as the electrolyte. Finally, the anodic layer is sealed through a standard NiF_2 cold-sealing procedure as described in the recent literature [38]. It is important to point out that the proposed anodizing and sealing procedures are commonly used at both an academic and industrial level and can be considered as a standard in the field.

2.3. Tensile and fatigue tests

Both tensile and HCF tests are performed using a servo-hydraulic testing system (Instron 8801) with a load cell of 100kN.

Tensile tests are conducted according to ISO 6892-1:2019 specification [37] on both non-anodized and anodized specimens at a constant strain rate of $0.00025s^{-1}$ at 22±0.5°C.

High-cycle fatigue (HCF) tests are performed on both non-anodized and anodized specimens according to ISO 1099:2017 standard [36] with an alternated sinusoidal loading (R=−1) at 22±0.5°C. The frequency of the applied sinusoidal stress is 20Hz. Three different stress amplitudes are investigated: 150, 130 and 110MPa. Load levels are chosen in order to obtain a linear Wöhler curve in the range between 150k and 1M cycles. Conditions for the end of HCF tests are break or runout (i.e. no failure after $5 \cdot 10^6$ cycles) of the specimens. The maximum number of performed cycles is chosen in accordance with literature [39-42]. N samples (N=10 in the case of non-anodized AlSi8Mg-T6 and N=6 in the case of anodized AlSi8Mg-T6) are tested for each stress amplitude. 90% confidence intervals for the populations of results are computed under the assumption of lognormal

distribution of fatigue lifetimes. Median values for each stress amplitude are used for the calculation of Basquin's equation ($\sigma_a = \beta \cdot N^{-\alpha} \rightarrow Log\ \sigma_a = Log\ \beta - \alpha\ Log\ N$, where N is the fatigue lifetime and σ_a the stress amplitude) via a regression analysis based on least-square method [43].

One-way ANOVA tests with a significant level of 0.1 are implemented in order to perform a statistical analysis between the populations of non-anodized and anodized samples. In the case of HCF results, the tests are performed for each stress level, by assuming a normal distribution of Log(N).

2.4. Roughness and microstructural characterization

The surface roughness before and after anodizing of Fy HCF samples is measured using a Leica DCM8 microscope equipped with an interferometric objective (green light, 20X). Images are acquired over 10 areas of $0.66 \times 0.877 mm^2$ along the gauge length of HCF specimens. The obtained pictures are then analysed using a Leica Map software and statistically treated.

In order to investigate the microstructure of the bulk material, six metallographic samples are obtained by sectioning of non-anodized and anodized HCF specimens along parallel and transversal directions. Specimens are then: 1) hot-mounted with phenolic resin; 2) ground with SiC papers with progressively higher grades (P800, P1200, P2400/4000); 3) polished with diamond pastes of 3μm and 1μm; and 4) chemically polished with a colloidal silica suspension (0.03μm). Samples are analysed with a Leica DM6 metallographic microscope under bright field light. Firstly, secondary dendrite arm spacing (SDAS) is measured according to the following equation: SDAS=L/(N-1) [44], where L is the total length between the middle of the first and the middle of the last arms of a single dendrite and N the number of intercepted arms. For each sample, an average over 10 dendrites is performed.

Secondly, the percentage of areal porosity (P%) is evaluated as the average over 20 images (optical magnification 5X). Moreover, the shape factor (SF) of the five largest pores is calculated by dividing the major axis and the minor axis of the ellipse that circumscribes each porosity. The mean dimension of the five largest pores (D_{5P}) is also evaluated by averaging the major and minor axes.

Finally, the mean dimension of eutectic Si particles (D_{Si}) and intermetallic particles (D_{int}) is evaluated as the square root of the corresponding area divided by the number of observed particles on 3 images taken at a magnification of 50X. The 3 images are selected in order to have at least 5 intermetallic and 20 Si particles in each image so to obtain statistically significant values from the measurement.

In order to evaluate the grain size (L_{grain}) of the AlSi8Mg-T6 alloy, metallographic samples are electrochemically etched with Barker's solution ($1.2\%_{vol}$ $HBF_{4(aq)}$). In details, Barker's etching is performed by applying a constant voltage of 25V for 180s. Electrochemically etched samples are then observed under polarized light as per ASTM E112-13 (Heyn linear intercept procedure) [45].

2.5. Instrumented micro-indentation test

Instrumented micro-indentation is implemented to perform measurements of the Vickers' micro-hardness on the cross-sections of bulk AlSi8Mg-T6 alloy and the anodic layer. A metallographic sample of anodized AlSi8Mg-T6 cut along the parallel direction is used for the test (see Paragraph 2.4). The parameters for the micro-indentation analysis are listed hereafter: a) maximum applied load equal to 200mN, b) load and unload rate equal to 400mN/min; c) 2s pause at the maximum load; and d) 100µm Vickers' indenter. A total of 5 indentations is carried out for both the bulk and the anodic layer. The analyses are performed with a MCT^3 (Anton Paar).

2.6. Analysis of fatigue fracture surfaces

Fatigue fracture surfaces are firstly sonicated in ethanol to remove eventual impurities and dust residual particles. Secondly, samples are: a) analysed under a stereo microscope to identify the distinct fracture regions; and b) inspected by means of a scanning electron microscope (SEM) with an operating voltage of 20kV. Morphological analysis is performed by using secondary electrons in depth and/or resolution modes with a probe current of 200pA. For anodized fatigue fracture surfaces, back-scattered electrode (BSE) images are also collected (probe current equals to 200pA). Qualitative compositional EDXS analysis (both on fatigue fracture surfaces and external surface of HCF specimens) is carried out by applying a probe current of 300pA in resolution mode and using an optimal working distance of 8.5mm. Cross-section of fatigue fracture surfaces is: a) obtained

following the same metallographic sample preparation described in Paragraph 2.4.; and b) analysed with a Leica DM6 metallographic microscope under bright field light.

3. Results and discussion

The effect of the anodic layer on the fatigue performance of the investigated AlSi8Mg-T6 alloy is studied by means of a multi-technique approach on anodized and non-anodized specimens. The following general approach is adopted: 1) composition (Paragraph 3.1), microstructure (Paragraph 3.2) and roughness (Paragraph 3.3) of samples are primarily investigated in great detail; 2) subsequently, specimens are characterized using tensile tests (Paragraph 3.4); 3) finally, high cycle fatigue measurements (Paragraph 3.5) and fracture surface analysis are carried out (Paragraph 3.6).

3.1. Elemental analysis of AlSi8Mg-T6

The chemical composition of the investigated AlSi8Mg-T6 alloy is probed using μ-XRF measurements as described in Paragraph 2.1. It is concluded that the material consists of an Aluminium-Silicon alloy, whose composition is reported in Table 1.

On the basis of the alloy composition, it is possible to infer the presence of eutectic Silicon particles as well as Iron-based precipitates, whose careful assessment is discussed in Paragraph 3.2.

Table 1. Chemical composition of AlSi8Mg-T6 alloy

	Weight %					
Alloy	**Si**	**Mg**	**Fe**	**Ti**	**Sr**	**Al**
AlSi8Mg-T6	8.1±0.4	0.15±0.03	0.109±0.005	0.14±0.02	0.004±0.001	balance

It is observed that AlSi8Mg-T6 shows a constant composition with only minor fluctuations in the alloying element concentrations. This point seems fundamental in order to exclude any effect of the alloy composition on fatigue performance.

3.2. Microstructure

3.2.1 Bulk AlSi8Mg-T6 alloy

The careful microstructural characterization of AlSi8Mg-T6 (see Paragraph 2.4) allows to calculate several figures of merit. Since non-anodized and anodized AlSi8Mg-T6 specimens are obtained from

the same casting batch (see Paragraph 2.1), no differences in the measured microstructural parameters are expected between these two groups of samples. Results are summarised in Table 2.

<div align="center">Table 2. Metallographic figures of merit of AlSi8Mg-T6.</div>

AlSi8Mg-T6		
SDAS	25 ± 3	µm
L_{grain}	397 ± 98	µm
P%	0.16 ± 0.10	%
D_{5P}	84 ± 40	µm
SF	2.2 ± 0.8	
D_{Si}	3.4 ± 0.3	µm
D_{int}	3.5 ± 0.8	µm

SDAS (secondary dendritic arm spacing), L_{grain} (grain size), P% (areal percentage of porosity), D_{5P} (mean dimension of the 5 largest pores), SF (mean shape factor of the 5 largest pores), D_{Si} (mean dimension of the eutectic Silicon particles), D_{int} (mean dimension of intermetallics)

It is possible to observe that AlSi8Mg-T6 consists of a typical T6-treated hypoeutectic cast AlSi*x* alloy [46] with spherodized Si particles, fine microstructure and good grain refinement (see Fig. 1) [46,47]. As a qualitative comment, in agreement with the low Iron content ([Fe]≤0.11%wt), the size (D_{int}) and concentration of Iron-rich intermetallic precipitates are small if compared with highly alloyed materials [48]. On the contrary, eutectic Silicon particles are clearly visible and highlight a well-defined dendritic structure (see Fig. 1a and Fig. 1b).

As reported in Fig. 1a, few microporosities are present within the AlSi8Mg-T6 matrix. These are predominantly of interdendritic shrinkage type and characterized by elongated and complex shapes [49].
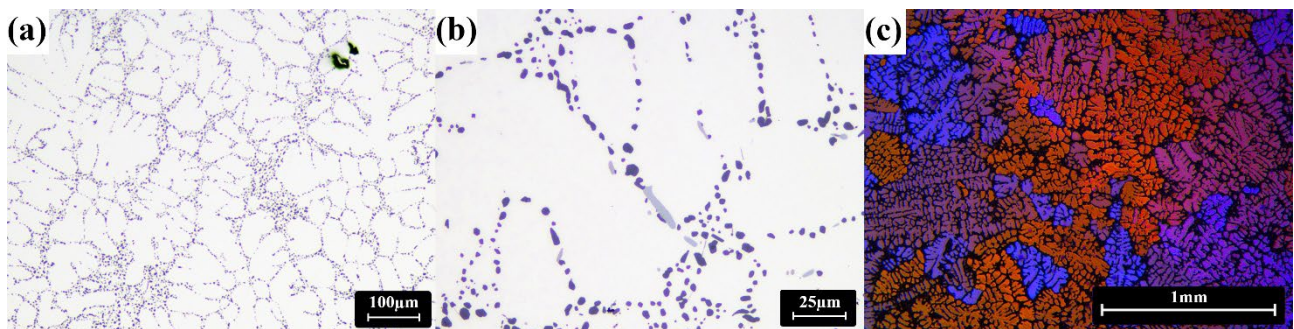

Fig. 1. Metallographic images of the investigated AlSi8Mg-T6 alloy at different magnifications ((a) and (b)); (c) Metallographic image under polarized light as obtained after Barker's etching for grain size evaluation. In (b), eutectic Si particles appear purple, while Fe-rich intermetallic particles appear grey.

3.2.2 Anodic layer

Specimens for tensile and fatigue tests are anodized as described in Paragraph 2.2. Cross-section metallographic analyses are performed on samples obtained from sectioning of HCF specimens, and confirm the growth of a 15μm-thick anodic layer (see Fig. 2). As clearly visible in Fig. 2a, the oxide layer shows a good thickness homogeneity and compactness with: a) no pitting phenomena at the interface between oxide and base alloy; and b) minor thickness reduction in correspondence of highly concentrated Si regions. This superior morphology is attributed to both: 1) the use of an optimized anodizing process as described in the recent literature [10,31]; and 2) a low (<0.15%) concentration of noble elements (e.g. Fe and Cu) which could undergo to dissolution phenomena upon anodizing [17]. Indeed, it is demonstrated that a careful tuning of the anodizing waveform allows to mitigate the adverse effect of intermetallic and eutectic Si particles on the coating homogeneity [9,10,34]. Specifically, the use of a pulsed square current waveform allows a proper embedding of Silicon particles (see Fig. 2b, green arrow) within the oxide layer, which otherwise lead to a pronounced local thickness fluctuation due to the negligible anodizability of Si particles [10,34]. In Fig. 2b it is also possible to detect the presence of a micro-void adjacent to an embedded Si particle (see light blue arrow). This kind of defect is related to gas evolution phenomena typically observed during the anodizing of AlSi*x* alloys [15,17].
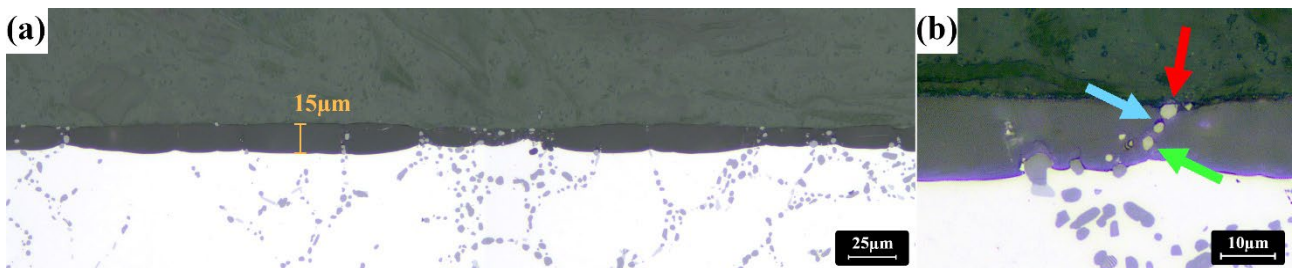

Fig. 2. (a) Overview and (b) detail at high magnification of the oxide layer with an emerging Si particle (red arrow), several embedded Si particles (green arrow) and a micropore (light blue arrow) associated with gas evolution in correspondence of Si particles.

SEM/EDXS analysis (Fig. 3) on the external surface of anodized HCF specimens shows the presence of emerging eutectic Si particles and micro-cracks (see Fig. 3b), which are not present prior to

anodizing (see Fig. 3a). In agreement with the literature [24,50], the presence of cracks on the surface of the anodic layer can be associated with the anodic layer sealing process. Indeed, the sealing process consists in the occlusion of the nano-pores of the anodic layer by means of a hydrothermal process which lead to the precipitation of oxides and hydroxides within the nano-pores. The nucleation and growth of the sealing phases within the oxide nano-pores, can lead to the generation of internal stresses with an associated cracking of the oxide layer [4,7,50]. It is interesting to observe that, after fatigue testing, the length and networking of these micro-cracks increase (see Fig. 3c) thus supporting the fact that the oxide micro-cracks can behave as triggers for fatigue crack and local surface stress raisers. The formation of a network of micro-cracks at the notch root of anodized, cast AlSi10Cu4Mg samples is also reported by Nakamura et al. [31]. Moreover, cracking of the anodic layer due to cycling loading is also commonly observed in the case of anodized wrought Aluminium alloys [11,16,18,21,24]. Finally, it is worth mentioning that no clear correlation between the presence of emerging Si particles (see Fig. 3b) and crack formations seems evident. This further confirms that the formation of cracks is strongly correlated with the anodic layer sealing process.

To further characterize the anodic layer, micro-indentation tests are carried out as described in Paragraph 2.5. It is important to highlight that this kind of analysis has a comparative meaning and absolute values are representative of the specific set of parameters used to perform the instrumented indentation test. Hence, the results on the anodic layer are reported in Table 3 in comparison to the one obtained with the same testing condition on bulk AlSi8Mg-T6 alloy. It is evident that the anodic layer is characterized by a hardness more than 3 times higher than the hardness of the bulk AlSi8Mg-T6 alloy. This result is in accordance with the literature [19] and it is a proof of the dissimilarity in the mechanical responses of the anodic layer with respect to bulk AlSi8Mg-T6 alloy. Moreover, it is interesting to report that during indentation tests the anodic layer shows brittleness, since cracking (see Fig. S1) occurred in 2 cases, forcing the invalidation and repetition of those indentations. This phenomenon is not observed for bulk AlSi8Mg-T6.

Table 3. Vickers hardness as obtained by instrumented micro-indentation.

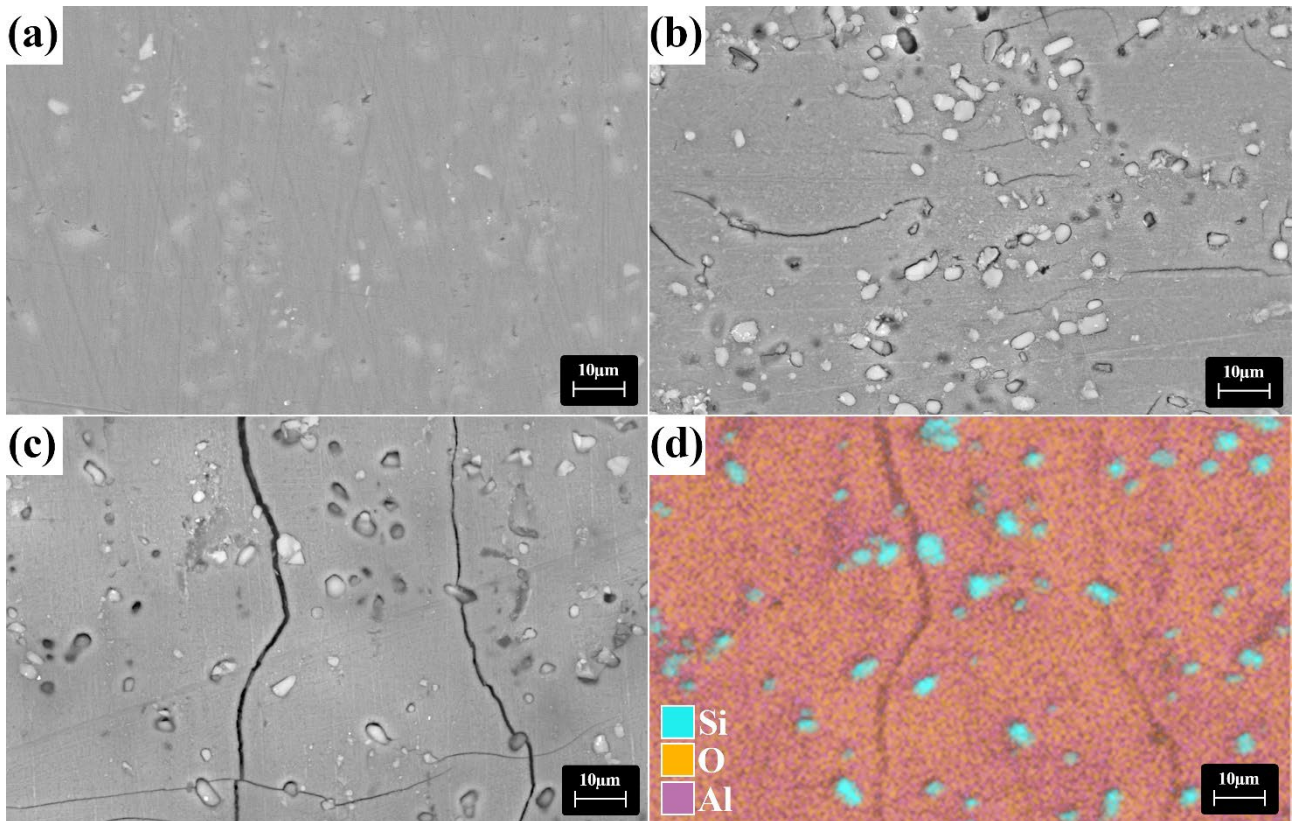| Hardness AlSi8Mg-T6		
Bulk	150 ± 4	HV
Anodic Layer	509 ± 3	HV

Fig. 3. (a) BSE-SEM images of the surface of specimens before anodizing; (b) after anodizing and before HCF measurement; (c) after anodizing and after HCF test in close proximity of the fracture surface; and (d) EDXS map of region (c). The EDXS map highlights emerging Silicon particles.

3.3. Roughness

The roughness of HCF specimens prior and after the anodizing process is evaluated as described in Paragraph 2.4. Results are reported in Fig. 4 in terms of roughness of each specimen and average values. Comparable values of areal roughness are obtained within the two analysed groups of samples. Any fluctuations in the acquired values can be ascribed to the local nature of the measurement. Among all the anodized HCF specimens, F2 sample exhibits a lower value of Sa; yet, this value can be considered to be within the typical areal roughness of anodized cast AlSi*x* alloys [10].
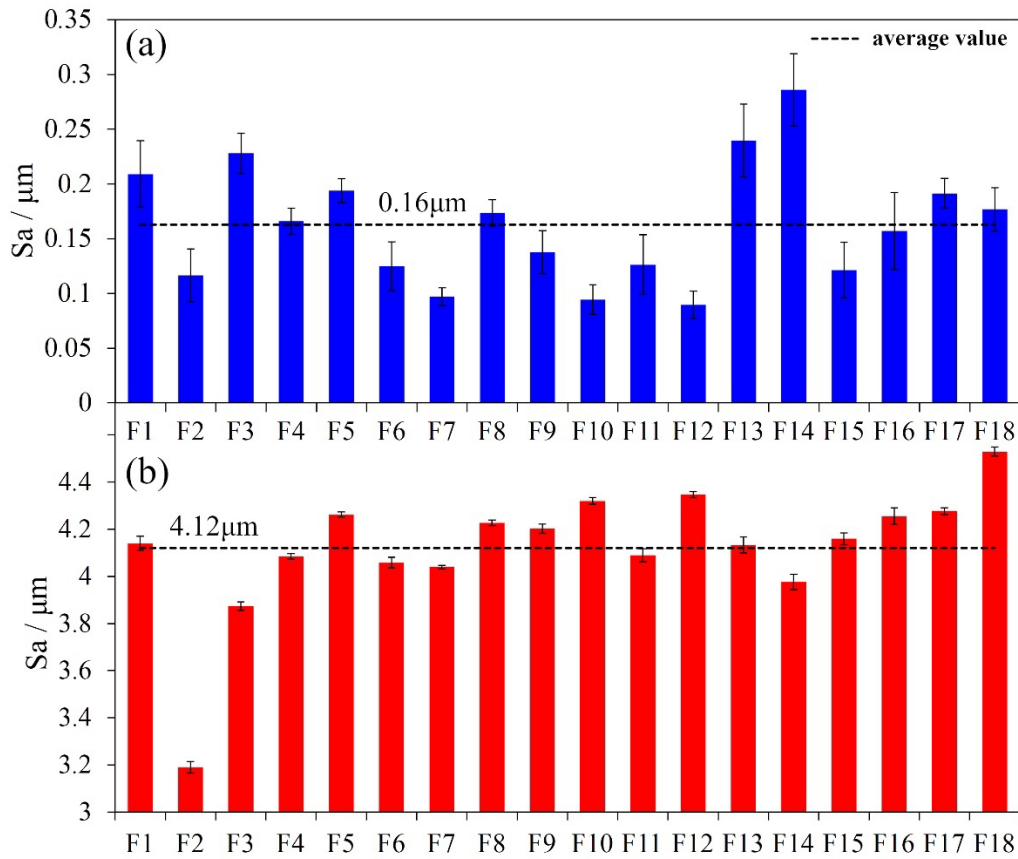
Fig. 4. Areal roughness (Sa) of HCF specimens before (a) and after (b) anodizing (the average value is represented by the dashed line). An increase of the surface roughness upon anodizing is clearly visible.

It is evident that, prior to anodizing, specimens show an average roughness equal to 0.16μm while, after anodizing, the average roughness increases up to 26 times, approaching 4.12μm. This phenomenon is related to the local microstructure of AlSi8Mg-T6. Indeed, the oxide growth is inhibited in those regions in which a high concentration of eutectic Si particles is present [14]. Hence, the oxide growing rate is higher on Al dendrite with respect to eutectic inter-dendritic regions. This results in a non-homogeneous growth of the oxide, thus leading to an increase in the surface roughness of specimens [10,17,34]. Moreover, emerging Si particles (see Fig. 3b) are likely to further contribute to the increase in the surface roughness. It is reasonable to infer that, due to this local notch effect, the surface of anodized specimens may be more susceptible to crack nucleation when subjected to cyclic loads [51].

3.4. Tensile characterization

Tensile properties of anodized AlSi8Mg-T6 specimens are investigated as described in Paragraph 2.3. Results of non-anodized AlSi8Mg-T6 are discussed as well. Data are summarized in Table 3 and Table 4 in terms of yield strength ($R_{p0.2}$), ultimate tensile strength (UTS) and elongation at fracture (A%).

Table 3. Tensile properties of non-anodized AlSi8Mg-T6 alloy.

Specimen	$R_{p0.2}$ / MPa	UTS / MPa	A% / %mm/mm
P1	292	341	5.7
P2	283	336	9.1
P3	299	350	10.5
P4	294	345	10.0
P5	293	345	9.0
Mean value	292	343	8.9
St. Dev.	6	5	1.9

$R_{p0.2}$: Yield strength; UTS: Ultimate tensile strength; A%: elongation at fracture

Table 4. Tensile properties of anodized AlSi8Mg-T6 alloy.

Specimen	$R_{p0.2}$ / MPa	UTS / MPa	A% / %mm/mm
A1	292	343	8.2
A2	284	336	7.4
A3	295	347	9.8
A4	296	344	5.9
A5	302	345	3.2
Mean value	294	343	6.9
St. Dev.	7	4	2.5

$R_{p0.2}$: Yield strength; UTS: Ultimate tensile strength; A%: elongation at fracture

Yield strength is equal to 292MPa for non-anodized specimens and 294MPa for anodized samples and, similarly, no differences in the UTS are observed, with values for both anodized and non-anodized alloys in the order of 343MPa. On the contrary, differences in the mean values of elongation at fracture are detected (8.9% *vs*. 6.9% for non-anodized and anodized specimens, respectively). The data dispersion in the case of A% is remarkably higher than that of R_p0.2 and and UTS and can be attributed to the presence of inhomogeneities in the AlSi8Mg-T6 microstructure, i.e. microporosities and intermetallic particles [52].

As expected, the presence of an anodic layer on sample surfaces has a negligible effect on strengths. Indeed, it is generally agreed that these properties are mostly dictated by the bulk microstructure of samples [2,48,53]. Specifically in the case of AlSix alloys, both $R_{p0.2}$ and UTS are significantly affected by: a) modification of eutectic Si particles; and b) performed thermal treatment which is responsible for the formation of Mg_2Si nano-precipitates with an associated hindrance of the dislocation motion [2,35,47]. Consistently, since both non-anodized and anodized samples undergo the same casting process and thermal treatment, no differences in $R_{p0.2}$ and UTS are to be expected. On the other hand, the difference in the elongation at fracture (A%) between anodized and non-anodized samples might be ascribed to the presence of the brittle and hard oxide layer [13,25,54]. Nonetheless, it is important to mention that from a statistical point-of-view the tensile properties (both A% and strengths) of non-anodized and anodized AlSi8Mg-T6 are equal, as verified by one-way ANOVA tests.

3.5. High cycle fatigue (HCF) measurements

High cycle fatigue (HCF) measurements on non-anodized and anodized specimens are performed as described in Paragraph 2.3. Results are reported in terms of fatigue life as a function of the stress amplitude (Fig. 5) and Basquin's fit (Fig. 6). No evidence of a fatigue limit (absence of runout specimens) is found for both non-anodized and anodized specimens. This is in contrast with what reported for anodized Aluminium alloys in other articles [16,18,24,27,28,30,31]. Yet, this dissimilarity might be related to: a) the different HCF testing procedures; b) the studied Aluminium alloys; and c) the applied anodizing parameters.

One-way ANOVA tests confirm that the populations of non-anodized and anodized HCF specimens are statistically different for both 130 and 110MPa stress amplitudes. Conversely, at 150MPa the two sets of samples are statistically equal. This behaviour can be understood in light of fatigue principles. Indeed, from a theoretical point of view, as the applied stress amplitude decreases (e.g. from 150MPa to 130 and 110MPa), the time required for the nucleation of the fatigue crack becomes progressively more relevant than the propagation time [43]. Hence, the presence of superficial features, which can

accelerate the fatigue crack nucleation, is expected to mostly impact the HCF behaviour at lower stress amplitudes.

In this specific case: a) the presence of the anodic layer increases the roughness of the specimens (see Paragraph 3.3) with an associated stress intensification effect [9,10,51]; b) local stresses might build up as a result of the difference in mechanical behaviours of the anodic layer and bulk AlSi8Mg-T6 matrix (see Paragraph 3.2.2) [16,18,24]; c) the brittle oxide layer can easily crack as a result of the applied cyclic stress (see Fig. 3c) [11,13,16,17]; and d) the anodic layer is characterized by microcracks induced by the oxide sealing process (see Fig. 3b) [10-16,18,24,31,50]. All of these aspects can facilitate the fatigue crack nucleation at the surface of anodized AlSi8Mg-T6 specimens, i.e. reduce the nucleation time. In terms of HCF tests, this becomes particularly evident at stress amplitudes of 130 and 110MPa.

As a consequence, as shown in Fig. 6, the linear Basquin's fits of the median values of non-anodized and anodized HCF specimens highlight a significant difference in the slopes. Specifically, the Basquin's equation of anodized samples has a more negative slope coefficient with respect to non-anodized specimens.
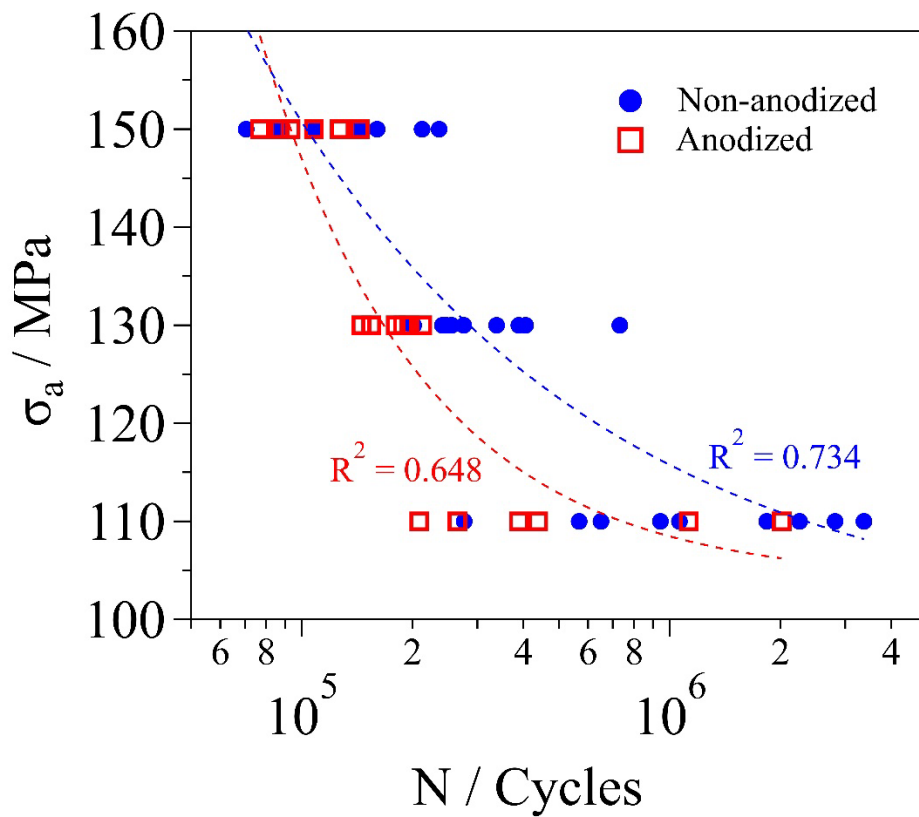
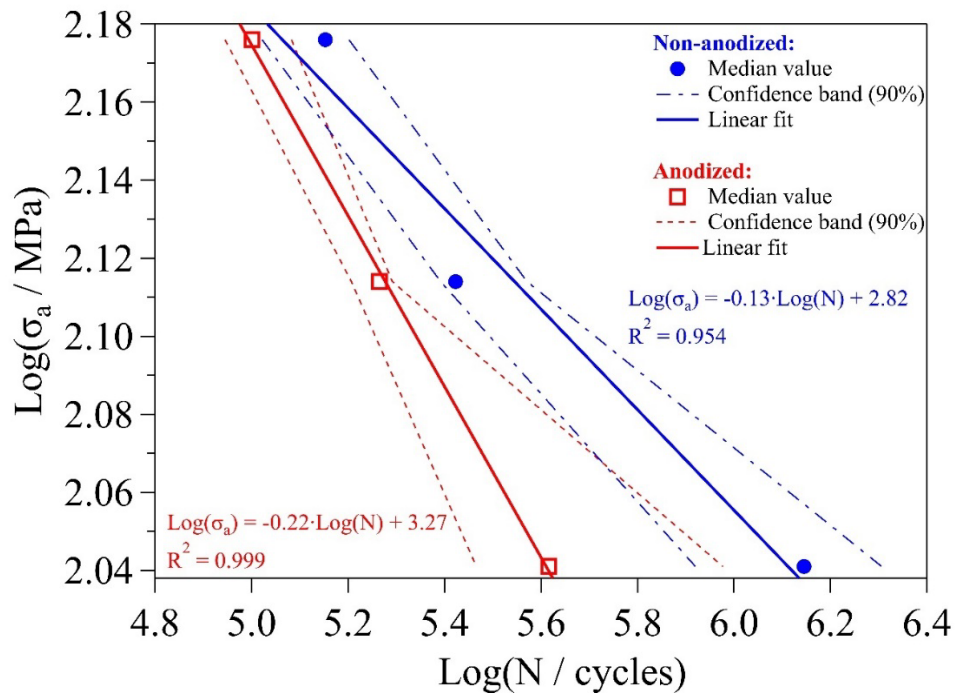**Fig. 5.** HCF results of non-anodized (blue dots) and anodized (red squares) specimens.

Fig. 6. Basquin's fits for non-anodized and anodized HCF samples (solid lines) and 90% confidence intervals of the experimental points as obtained by assuming a normal distribution of $Log_{10}(N)$.

Careful investigations of: a) the nucleation mechanisms of fatigue cracks at different stress levels; and b) the differences in the crack nucleation mechanisms between non-anodized and anodized samples are completed by studying the fracture surfaces of specimens after HCF measurements. The results are presented in the following section.

3.6. Fracture surfaces analyses

3.6.1. Non-anodized specimens

HCF fracture surfaces are investigated by means of a scanning electron microscope (SEM) as described in Paragraph 2.6. As an example, Fig. 7 shows three representative fracture surfaces of non-anodized AlSi8Mg-T6, one for each stress amplitude level (110, 130 and 150 MPa).
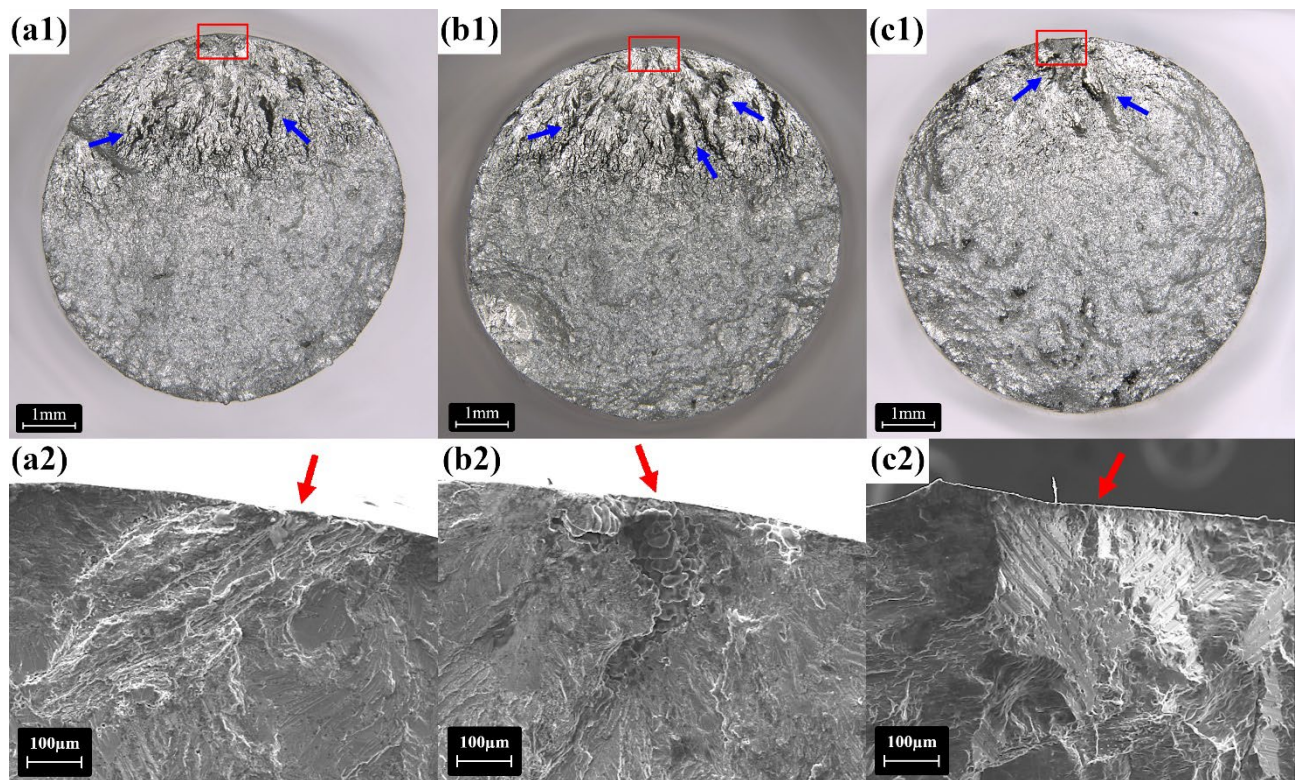

Fig. 7. Examples of fracture surfaces of non-anodized AlSi8Mg-T6 at different stress levels: (a1) and (a2) 110MPa; (b1) and (b2) 130MPa; (c1) and (c2) 150MPa. Red arrows indicate the nucleation sites.

All the inspected fracture surfaces (see Fig. 7 and supplementary Fig. S2) exhibit three well distinguishable zones: nucleation site (see red boxes and red arrows), stable propagation zone (characterized by the presence of tear ridges, blue arrows) and final fast propagation zone (overload failure). In addition, a careful investigation of the fracture surfaces, combined with EDXS analysis,

allows to identify the following characteristics in correspondence of crack nucleation sites: a) sub-surface shrinkage porosity (Fig. 7b2); b) decohesion of eutectic regions associated with entrapped oxide layers (Fig. 7a2) and Fig. S3); and c) slip bands of Al matrix (Fig. 7c2 and Fig. S4), which suggest a ductile mechanism of fatigue crack nucleation, induced by the dislocation motion along preferential crystalline planes of the Al matrix [55,56].

Among these features, microporosity is detected in correspondence of the nucleation site of the majority of the investigated specimens, thus indicating that the failure mechanism of the non-anodized AlSi8Mg-T6 alloy is mostly driven by superficial micro-shrinkage pores (casting defects) which trigger the crack nucleation [26,57,58].

3.6.2. Anodized specimens

The fracture surfaces of anodized specimens are investigated in order to identify the effect of the presence of a surface anodic layer (see Paragraph 3.2.2) on the fatigue life of AlSi8Mg-T6. Three fracture surfaces per stress level are investigated by using SEM-based methods (see Paragraph 2.6). Results are summarized in Fig. 8 and Fig. S5.
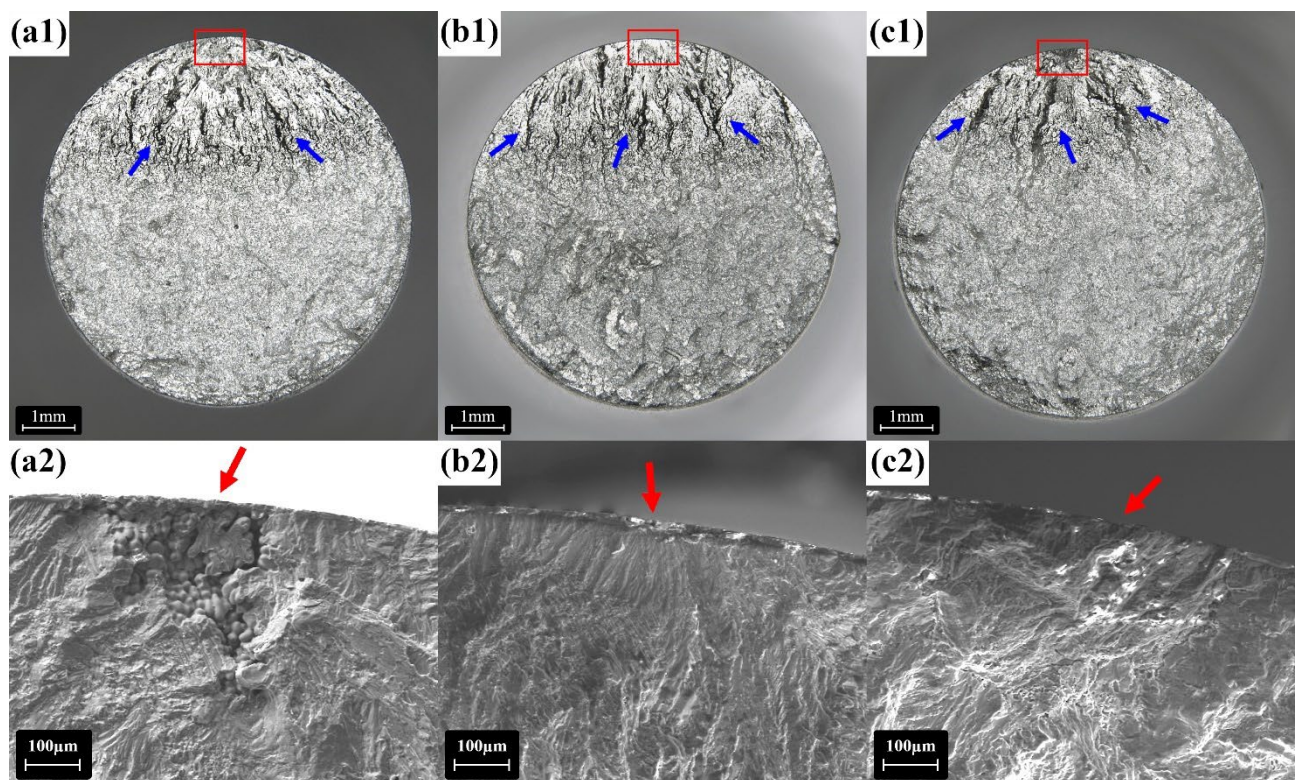
Fig. 8. Examples of fracture surface of anodized AlSi8Mg-T6 at different stress levels: (a1) and (a2) 110MPa; (b1) and (b2) 130MPa; (c1) and (c2) 150MPa. Red arrows indicate the nucleation sites.

Three relevant examples of fracture surfaces are reported in Fig.8. It is possible to observe that nucleation (see red box and red arrows), propagation (characterized by the presence of tear ridges, see blue arrows) and final failure regions are clearly visible. Similarly to non-anodized specimens, the fatigue nucleation occurs in correspondence of: a) micro-porosity (see Fig. 8a2); b) slip bands (see Fig. 8b2); and c) entrapped oxide (see Fig. 8c2). However, the morphology of nucleation sites associated with slip bands of the matrix in anodized samples is strongly different with respect to non-anodized ones. By looking at Fig. 8b2 and Fig. 7c2, respectively, it is clear that, in its early lifetime, the fatigue crack in anodized AlSi8Mg-T6 sample propagates in a less tortuous way with respect to its non-anodized counterpart. In order to further elucidate this aspect, one of the two fracture surfaces of F8 anodized fatigue specimen (see Fig. S5e) is cut, polished and analysed under the optical microscope (see Paragraph 2.6). An overview of the cross-section is reported in Fig. 9. It is clear that at the nucleation site and in the early propagation region, the fatigue crack path is extremely flat. Moreover, it is also possible to observe that: 1) as the fatigue crack proceeds, secondary fatigue cracks are detected, and 2) final failure due to overload is associated with severe plastic deformation of the Al matrix. These last two points are in agreement with what reported in literature for cast AlSix alloys [59,60].

Fig. 9. Cross-section of the fatigue fracture surface of F8 HCF specimen with details of: the nucleation site (red box), a secondary fatigue crack in the propagation region (yellow box) and severe plastic deformation of the Al matrix during the final failure region (light blue box).

A close-up on fracture surfaces highlights that fatigue crack originates from regions in which the oxide appears damaged (see red box in Fig. 10). Once the defected, brittle anodic layer fails due to the applied cyclic stress, the fatigue crack propagates into the Al matrix. However, due to the constrain imposed by the anodic layer at the surface, in the early-life stage of the fatigue crack growth, the motion of dislocations toward the fatigue crack tip is hindered [11,13]. As a consequence, the fatigue crack propagation requires less energy and proceeds faster, thus shortening the fatigue life of the alloy.

This behaviour is compatible with the hardness and brittle nature of the anodic layer [11,13,20,25], whose micro-cracks (see Paragraph 3.2.2) and intrinsic roughness (see Paragraph 3.3) can intensify the applied fatigue stress at the surface of anodized AlSi8Mg-T6 specimens [11,16,24,51].
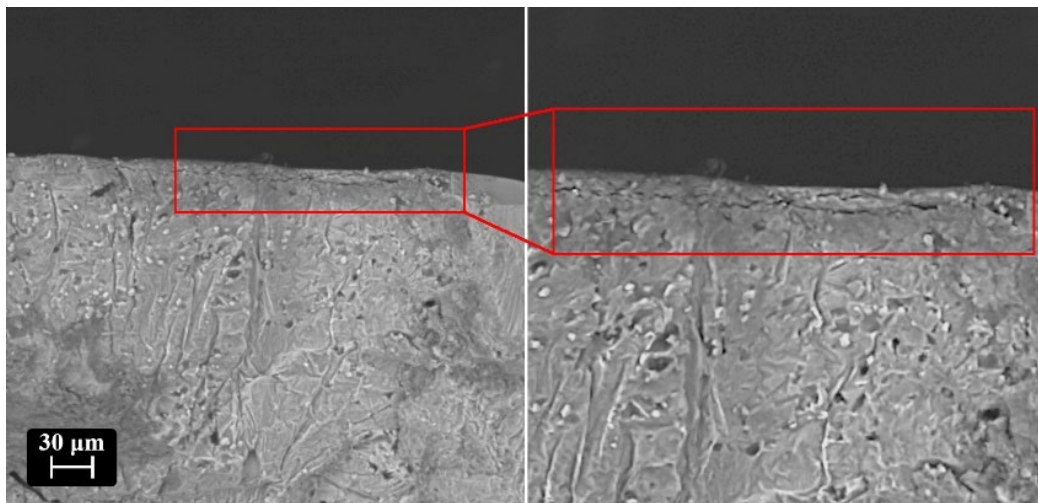

Fig. 10. BSE-SEM image and detail of multiple initiation sites from an eutectic Si-rich zone (specimen F6, cycled at 130MPa) of anodized AlSi8Mg-T6 samples. White round precipitates are eutectic Si particles.
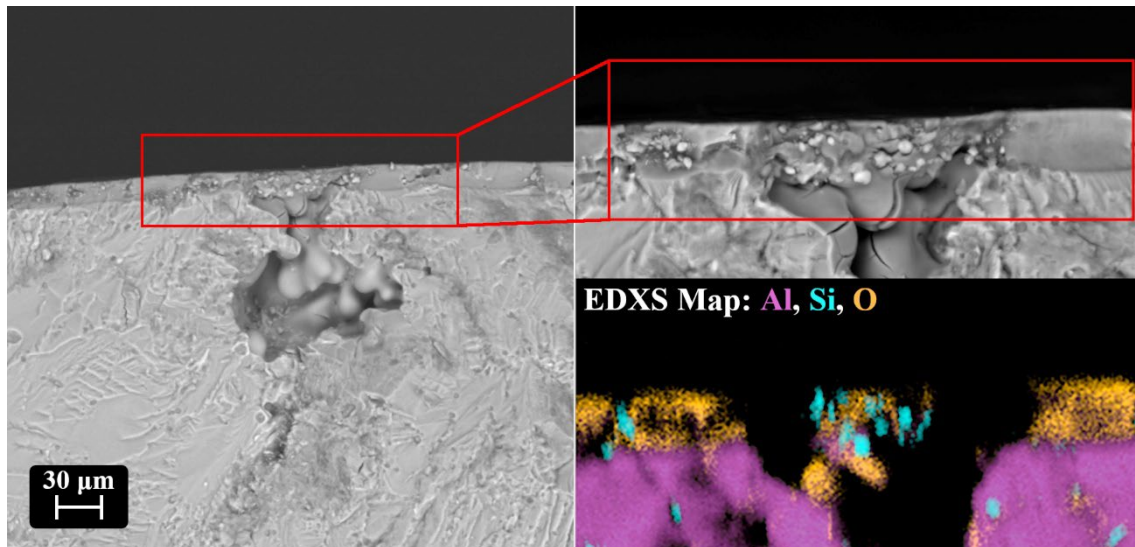
Fig. 11. BSE-SEM image and detail of fatigue initiation site from a small pore (specimen F9, cycled at 110MPa). The EDXS map of the detail of the initiation site is reported to highlight the presence of eutectic Si particles.

As a further failure mode, it is important to mention that micro-porosities covered by a highly defected oxide layer are also present in correspondence of crack nucleation sites. In particular, the anodic layer covering the pore comprises a high concentration of eutectic Si particles (see Fig. 11) which: a) creates a discontinuity on the oxide coating with a local stress build-up effect; and b) contributes to increase the local roughness of specimens (see Paragraph 3.3), thus generating a micro-notching effect at the specimen surface [51].

3.6.3. Propagation and final failure

Fig. 12 shows a comparison between two of the examined non-anodized and anodized surface fractures. The propagation zones of both non-anodized and anodized fracture surfaces are characterized by: tear ridges (purple arrows), secondary fatigue cracks (green arrow) and striations (see Fig. S6). It is also important to highlight that during propagation, casting defects (e.g. shrinkage pores, white arrows) are intercepted by the growing fatigue crack. On the other hand, the final failure zones of both non-anodized and anodized fracture surfaces show the presence of dimples (see yellow boxes and arrows), which are distinctive of a ductile failure mechanism. These features agree with what observed in the examined cross-section of anodized F8 sample (see Fig. 9, paragraph 3.6.2) and with cast AlSix alloys with similar chemical composition reported in the literature [59-64]. Thus, it

can be concluded that, in terms of propagation and final fracture behaviour, no significant differences are detected between non-anodized and anodized fracture surfaces. This further confirms that the effect of anodizing on fatigue performance is strictly related to changes in the fracture behaviour during the early life of the fatigue crack (i.e. initiation).

3.7. Effect of the anodic layer on fatigue life

By comparing HCF measurements and fracture surface analyses of non-anodized and anodized specimens, it is possible to conclude that the presence of an anodic layer strongly affects the fatigue response of cast AlSi8Mg-T6 specimens. In the case of non-anodized specimens, the mechanism of crack initiation is mostly related to the presence of surface microporosities. Indeed, casting defects (shrinkage, gas pores and entrapped oxides) are reported to be the main source for fatigue crack nucleation in cast AlSix alloys [30]. On the other hand, in the case of anodized specimens, the growth of a brittle, hard oxide layer on the surface of specimens is typically accompanied with: a) the presence of micro-cracks within the oxide causing a stress intensification effect (see Paragraph 3.2.2); b) a discontinuity in the mechanical behaviour of the surface with respect to the bulk alloy (see Paragraph 3.2.2); and c) the increase in the roughness of specimens due to the local thickness variation of the anodic layer (effect of Si-rich eutectic region) and the presence of emerging Silicon particles at the surface of the layer (see Paragraph 3.3). Taken altogether, these effects: a) strongly modulate the nucleation and early propagation of fatigue cracks; and b) reduce the fatigue lifetime of the AlSi8Mg-T6 alloy.

To sum up, although casting defects govern the nucleation of fatigue cracks in non-anodized specimens, the presence of an anodic layer alters this behaviour, worsening the overall fatigue performance of AlSi8Mg-T6 alloy. As a consequence, anodizing cannot be neglected and must be taken into consideration for a proper design of fatigue-resistant cast components.
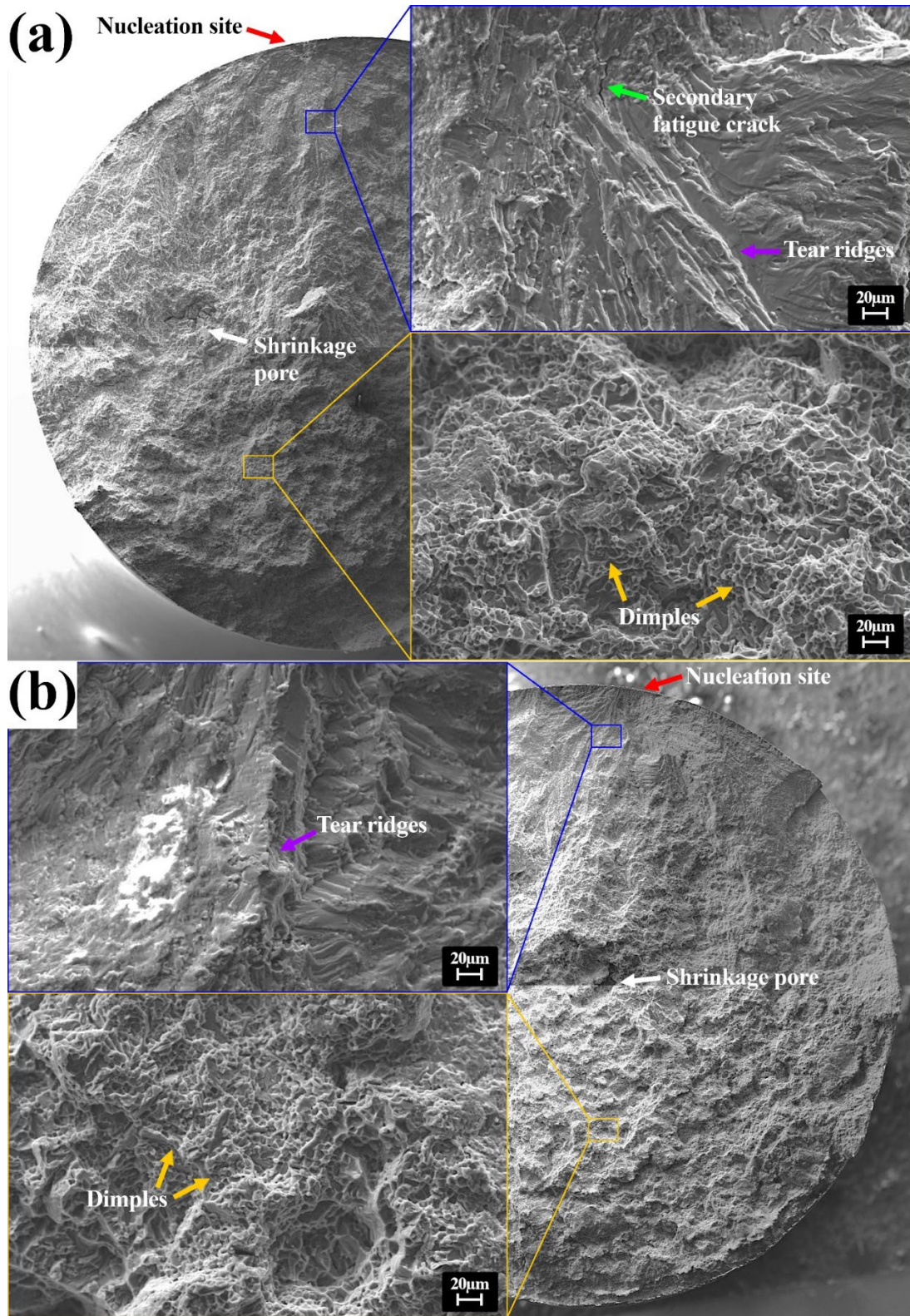
Fig. 12. Low magnification SEM images and details of propagation (blue boxes) and final failure zones (yellow boxes) of: (a) non-anodized P10 fracture surface and (b) anodized F12 fracture surface.

4. Conclusions

The manuscript investigates the effect of anodizing on the fatigue life of a cast AlSi8Mg-T6 alloy. A group of anodized specimens is prepared by using an *ad-hoc* anodizing process and tested with a multi-technique approach. The following conclusions are demonstrated:

- Anodizing increases the surface roughness of AlSi8Mg-T6 specimens. In particular, the surface roughness of anodized specimens is up to 26-times higher than non-anodized specimens (Sa<0.2μm).

- At 130 and 110MPa fatigue stress levels, anodizing significantly reduces the fatigue lifetime of AlSi8Mg-T6. Indeed, the slope of the linear Basquin's fit of anodized AlSi8Mg-T6 results significantly more negative than non-anodized AlSi8Mg-T6 (-0.22 *vs*. -0.13, respectively).

- In the case of non-anodized alloy, the fatigue nucleation mechanism is mainly associated with the presence of surface microporosities. On the other hand, in the case of anodized specimens, crack nucleation is associated with the brittle and hard nature of the oxide layer, which shows distinctive features such as micro-cracks, emerging and embedded Si particles and thickness reduction in correspondence of Silicon -rich eutectic regions. These features concur in modulating the nucleation and early propagation of cracks, with an overall reduction of fatigue life of the investigated AlSi8Mg-T6 alloy.

In conclusion, this work proves that, despite the presence of microstructural defects, (e.g. microporosities, entrapped oxides), anodizing has a negative effect on the fatigue resistance of cast AlSi8Mg-T6 alloy.

Moreover, on a broader perspective, the manuscript demonstrates that a careful physico-mechanical characterization can provide useful fatigue data to be used in the design of future anodized, cast AlSi*x* components.

Declaration of Competing Interest

The authors declare no competing financial interests.

References

[1] KEARNEY, A.; ROOY, Elwin L. Aluminum Foundry Products, Properties and Selection: Nonferrous Alloys and Special-Purpose Materials, Vol 2, ASM Handbook, By ASM Handbook Committee, ASM International, 1990, p 123–151, https://doi.org/10.31399/asm.hb.v02.a0001061.

[2] WANG, L.; MAKHLOUF, M.; APELIAN, D. Aluminium die casting alloys: alloy composition, microstructure, and properties-performance relationships. International Materials Reviews, 1995, 40(6): 221-238. https://doi.org/10.1179/imr.1995.40.6.221.

[3] WIELAGE, B.; ALISCH, G.; LAMPKE, T.; NICKEL, D.. Anodizing–a key for surface treatment of aluminium. In: Key Engineering Materials. Trans Tech Publications Ltd, 2008. p 263-281. https://doi.org/10.4028/www.scientific.net/KEM.384.263.

[4] RUNGE, J. M. Anodizing, Aluminum Science and Technology, Vol 2A, ASM Handbook, Edited By ANDERSON, K.; WERITZ, J.; KAUFMAN, J. G. ASM International, 2018, p 590–605, https://doi.org/10.31399/asm.hb.v02a.a0006523.

[5] MOON, S. M.; PYUN, S. I. A Review of Anodizing of Aluminium, 1997, 26: 498-508.

[6] THOMPSON, G. E.; HABAZAKI, H.; SHIMIZU, K.; SAKAIRI, M.; SKELDON, P.; ZHOU, X.; WOOD, G.C. Anodizing of aluminium alloys. Aircraft Engineering and Aerospace Technology, 1999, 71(3): 228-238. https://doi.org/10.1108/00022669910270709.

[7] PAZ MARTÍNEZ-VIADEMONTE, M.; ABRAHAMI, S. T.; HACK, T.; BURCHARDT, Malte; TERRYN, H. A review on anodizing of aerospace aluminum alloys for corrosion protection. Coatings, 2020, 10(11): 1106. https://doi.org/10.3390/coatings10111106.

[8] PATEL, P.; PATEL, T. Coloring Anodized Aluminum, Aluminum Science and Technology, Vol 2A, ASM Handbook, Edited By ANDERSON, K; WERITZ, J.; KAUFMAN, J. G. ASM International, 2018, p 611–615, https://doi.org/10.31399/asm.hb.v02a.a0006512.

[9] FRATILA-APACHITEI, L. E.; DUSZCZYK, J.; KATGERMAN, L. Voltage transients and morphology of AlSi (Cu) anodic oxide layers formed in H2SO4 at low temperature. Surface and Coatings Technology, 2002, 157(1): 80-94. https://doi.org/10.1016/S0257-8972(02)00144-5.

[10] FRATILA-APACHITEI, L. E.; DUSZCZYK, J.; KATGERMAN, L. AlSi(Cu) anodic oxide layers formed in H_2SO_4 at low temperature using different current waveforms. Surface and Coatings Technology, 2003, 165(3): 232-240. https://doi.org/10.1016/S0257-8972(02)00733-8.

[11] CREE, A. M.; WEIDMANN, G. W. Effect of anodised coatings on fatigue crack growth rates in aluminium alloy. Surface engineering, 1997, 13(1): 51-55. https://doi.org/10.1179/sur.1997.13.1.51.

[12] DE CAMARGO, J. A. M., CORNELIS, H. J., CIOFFI, Voorwald M. O. H.; COSTA, M. Y. P. Coating residual stress effects on fatigue performance of 7050-T7451 aluminum alloy. Surface and coatings technology, 2007, 201(24): 9448-9455. https://doi.org/10.1016/j.surfcoat.2007.03.032.

[13] HEMMOUCHE, L.; FARES, C.; BELOUCHRANI, M. A. Influence of heat treatments and anodizing on fatigue life of 2017A alloy. Engineering Failure Analysis, 2013, 35: 554-561. https://doi.org/10.1016/j.engfailanal.2013.05.003.

[14] FRATILA-APACHITEI, L. E.; TERRYN, H; SKELDON, P; THOMPSON, G. E.; DUSZCZYK, J.; KATGERMANA, L. Influence of substrate microstructure on the growth of anodic oxide layers. Electrochimica acta, 2004, 49(7): 1127-1140. https://doi.org/10.1016/j.electacta.2003.10.024.

[15] FRATILA-APACHITEI, L. E.; TICHELAAR, F.D; THOMPSON, G. E.; TERRYN, H.; SKELDON, P.; DUSZCZYK, J.; KATGERMAN, L. A transmission electron microscopy study of hard anodic oxide layers on AlSi (Cu) alloys. Electrochimica Acta, 2004, 49(19): 3169-3177. https://doi.org/10.1016/j.electacta.2004.02.030.

[16] WRAGG, D. A.; DAVIES, D. P.; JENKINS, S. L. Influence of and differences between Chromic and Sulphuric acid anodising on the fatigue properties of 7050 T7451 aluminium alloy. International Journal of Fatigue, 2022, 163: 107026. https://doi.org/10.1016/j.ijfatigue.2022.107026.

[17] SCAMPONE, G.; TIMELLI, G. Anodizing Al–Si foundry alloys: a critical review. Advanced Engineering Materials, 2022, 24(4): 2101480. https://doi.org/10.1002/adem.202101480.

[18] NIE, B.; ZHANG, Z.; ZHAO, Z.; ZHONG, Q. Effect of anodizing treatment on the very high cycle fatigue behavior of 2A12-T4 aluminum alloy. Materials & Design, 2013, 50: 1005-1010. https://doi.org/10.1016/j.matdes.2013.03.083.

[19] MUSZA, A.; UGI, D.; VIDA, Á.; CHINH, N. Q. Study of Anodic Film's Surface and Hardness on A356 Aluminum Alloys, Using Scanning Electron Microscope and In-Situ Nanoindentation. Coatings, 2022, 12(10): 1528. https://doi.org/10.3390/coatings12101528.

[20] SHAHZAD, M.; CHAUSSUMIER, M.; CHIERAGATTI, R.; MABRU, C.; REZAI ARIA, F. Influence of surface treatments on fatigue life of Al 7010 alloy. Journal of Materials Processing Technology, 2010, 210(13): 1821-1826. https://doi.org/10.1016/j.jmatprotec.2010.06.019.

[21] SHAHZAD, M.; CHAUSSUMIER, M.; CHIERAGATTI, R.; MABRU, C.; REZAI ARIA, F. Surface characterization and influence of anodization process on fatigue life of Al 7050 alloy. Materials & Design, 2011, 32(6): 3328-3335. https://doi.org/10.1016/j.matdes.2011.02.027.

[22] HALDERMAN, J. D., "Automotive Brake System, 7th Edition," Pearson, 2007, ISBN-13 9780134063126.

[23] BANDIERA, M.; MAURI, A.; BESTETTI, M.; BONFANTI, A.; MANCINI, A.; BERTASI, F. Corrosion phenomena in braking systems. NACE International, 2020, C2020-14550: 1-12.

[24] SHAHZAD, M.; CHAUSSUMIER, M.; CHIERAGATTI, R.; MABRU, C.; REZAI ARIA, F. Effect of sealed anodic film on fatigue performance of 2214-T6 aluminum alloy. Surface and coatings technology, 2012, 206(11-12): 2733-2739. https://doi.org/10.1016/j.surfcoat.2011.10.033.

[25] HEMMOUCHE, L.; FARES, C.; BELOUCHRANI, M. A. Influence of heat treatments and anodization on fatigue life of 2017A alloy. Engineering Failure Analysis, 2013, 35: 554-561. https://doi.org/10.1016/j.engfailanal.2013.05.003.

[26] WINTER, L.; LAMPKE, T. Influence of Hydrothermal Sealing on the High Cycle Fatigue Behavior of the Anodized 6082 Aluminum Alloy. Coatings, 2022, 12(8): 1070. https://doi.org/10.3390/coatings12081070.

[27] ZHU, W.; DENG, Y.; GUO, X. Influence of adjusting the anodizing and aging sequences on the microstructure, fatigue property and corrosion resistance of anodized AA6082 alloys. Materials Characterization, 2022, 189: 111941. https://doi.org/10.1016/j.matchar.2022.111941.

[28] DEL OLMO, R.; MOHEDANO, M.; VISSER, P.; RODRIGUEZ, A.; MATYKINA, E.; ARRABAL, R. Effect of cerium (IV) on thin sulfuric acid anodizing of 2024-T3 alloy. Journal of Materials Research and Technology, 2021, 15: 3240-3254. https://doi.org/10.1016/j.jmrt.2021.09.117.

[29] ATTOLICO, M. A.; CASAVOLA, C.; MORAMARCO, V.; RENNA, G.; FURFARI, D.; BUSSE, D. O. Influence of tartaric- sulfuric acid anodic film on four- point bending fatigue behavior of AA 7050- T7451 samples. Fatigue & Fracture of Engineering Materials & Structures, 2022, 45(12): 3716-3730. https://doi.org/10.1111/ffe.13844.

[30] RATEICK, R. G.; BINKOWSKI, T. C.; BORAY, B. C. Effect of hard anodize thickness on the fatigue of AA6061 and C355 aluminium. Journal of materials science letters, 1996, 15(15): 1321-1323. https://doi.org/10.1007/BF00240794.

[31] NAKAMURA, Y.; SAKAI, T.; HIRANO, H., RAVI CHANDRAN, K. S. Effect of alumite surface treatments on long-life fatigue behavior of a cast aluminum in rotating bending. International journal of fatigue, 2010, 32(3): 621-626. https://doi.org/10.1016/j.ijfatigue.2009.10.002.

[32] WANG, Q. G.; APELIAN, D.; LADOS, D. A. Fatigue behavior of A356-T6 aluminum cast alloys. Part I. Effect of casting defects. Journal of light metals, 2001, 1(1): 73-84. https://doi.org/10.1016/S1471-5317(00)00008-0.

[33] WANG, Q. G.; CREPEAU, P. N.; DAVIDSON, C. J.; GRIFFITHS, J. R. Oxide films, pores and the fatigue lives of cast aluminum alloys. Metallurgical and Materials Transactions B, 2006, 37(6): 887-895. https://doi.org/10.1007/BF02735010.

[34] BANDIERA, M.; PAVESI, A.; BESTETTI, M.; MANCINI, A.; BONFANTI, A.; BERTASI, F. Optimized Pulsed Anodization for Corrosion Protection of Aluminum Silicon Alloys. CORROSION 2021, NACE-2021-16431: 1-14.

[35] BANHART, J. Age Hardening of Aluminum Alloys, Heat Treating of Nonferrous Alloys, Vol 4E, ASM Handbook, Edited By TOTTEN, G. E., ASM International, 2016, p 214–239. https://doi.org/10.31399/asm.hb.v04e.a0006268.

[36] ISO 1099:2017. Metallic materials — Fatigue testing — Axial force-controlled method. Geneva: International Organization for Standardization.

[37] ISO 6892-1:2019. Metallic materials — Tensile testing — Part 1: Method of test at room temperature. Geneva: International Organization for Standardization.

[38] BANDIERA, M.; MANCINI, A.; PAVESI, A.; BONFANTI, A.; BESTETTI, M.; BERTASI, F. Lab-Scale Anodization of Prototype Brake Calipers. EUROBRAKE2021, EB2021-STP-012: 1-8.

[39] SONSINO, C. M.; ZIESE, J. Fatigue strength and applications of cast aluminium alloys with different degrees of porosity. International Journal of Fatigue, 1993, 15(2): 75-84. https://doi.org/10.1016/0142-1123(93)90001-7.

[40] LINDER, Jan. The influence of surrounding environment on the fatigue properties for a high pressure die cast AlSi9Cu3 alloy. Fatigue & Fracture of Engineering Materials & Structures, 2007, 30.8: 759-765. https://doi.org/10.1111/j.1460-2695.2007.01104.x.

[41] MU, P.; NADOT, Y.; NADOT-MARTIN, C.; CHABOD, A.; SERRANO-MUNOZ, I.; VERDU, C. Influence of casting defects on the fatigue behavior of cast aluminum AS7G06-T6. International Journal of Fatigue, 2014, 63: 97-109. https://doi.org/10.1016/j.ijfatigue.2014.01.011.

[42] SERRANO-MUNOZ, I.; BUFFIERE, J.-Y.; VERDU, C.; GAILLARD, Y.; MU, P.; NADOT, Y. Influence of surface and internal casting defects on the fatigue behaviour of A357-T6 cast aluminium alloy. International Journal of Fatigue, 2016, 82: 361-370. https://doi.org/10.1016/j.ijfatigue.2015.07.032.

[43] LEE, Y.-L.; PAN, J.; HATHAWAY, R.; BARKEY, M. "Fatigue testing and analysis: theory and practice," Elsevier Butterworth–Heinemann, 2005, ISBN 0-7506-7719-8.

[44] VANDERSLUIS, E.; RAVINDRAN, C. Comparison of measurement methods for secondary dendrite arm spacing. Metallography, Microstructure, and Analysis, 2017, 6(1): 89-94. https://doi.org/10.1007/s13632-016-0331-8.

[45] ASTM E112-13(2021). Standard Test Methods for Determining Average Grain Size. West Conshohocken: ASTM International.

[46] WANG, Q. G. Microstructural effects on the tensile and fracture behavior of aluminum casting alloys A356/357. Metallurgical and materials Transactions A, 2003, 34(12): 2887-2899. https://doi.org/10.1007/s11661-003-0189-7.

[47] ZHU, M.; JIAN, Z.; GENCANG, Y.; YAOHE, Z. Effects of T6 heat treatment on the microstructure, tensile properties, and fracture behavior of the modified A356 alloys. Materials & Design (1980-2015), 2012, 36: 243-249. https://doi.org/10.1016/j.matdes.2011.11.018.

[48] TAYLOR, J. A. Iron-containing intermetallic phases in Al-Si based casting alloys. Procedia Materials Science, 2012, 1: 19-33. https://doi.org/10.1016/j.mspro.2012.06.004.

[49] ANSON, J. P.; GRUZLESKI, J. E. The quantitative discrimination between shrinkage and gas microporosity in cast aluminum alloys using spatial data analysis. Materials characterization, 1999, 43(5): 319-335. https://doi.org/10.1016/S1044-5803(99)00059-5.

[50] LIU, W.; ZUO, Y.; CHEN, S.; ZHAO, X.; ZHAO, J. The effects of sealing on cracking tendency of anodic films on 2024 aluminum alloy after heating up to 300° C. Surface and Coatings Technology, 2009, 203(9): 1244-1251. https://doi.org/10.1016/j.surfcoat.2008.10.032.

[51] POMBERGER, S.; LEITNER, M.; STOSCHKA, M. Evaluation of surface roughness parameters and their impact on fatigue strength of Al-Si cast material. Materials Today: Proceedings, 2019, 12: 225-234. https://doi.org/10.1016/j.matpr.2019.03.118.

[52] MA, Z.; SAMUEL, A. M.; SAMUEL, F. H.; DOTY, H. W.; VALTIERRA, S. A study of tensile properties in Al–Si–Cu and Al–Si–Mg alloys: Effect of β-iron intermetallics and porosity. Materials Science and Engineering: A, 2008, 490(1-2): 36-51. https://doi.org/10.1016/j.msea.2008.01.028.

[53] SHIVKUMAR, S.; RICCI, S.; KELLER, C. Effect of solution treatment parameters on tensile properties of cast aluminum alloys. Journal of Heat Treating, 1990, 8(1): 63-70. https://doi.org/10.1007/BF02833067.

[54] LIU, F.; ZHAO, H.; YANG, R.; SUN, F. Crack propagation behavior of die-cast AlSiMgMn alloys with in-situ SEM observation and finite element simulation. Materials Today Communications, 2019, 19: 114-123. https://doi.org/10.1016/j.mtcomm.2019.01.009.

[55] SIEGFANZ, S.; GIERTLER, A.; MICHELS, W.; KRUPP, U. Influence of the microstructure on the fatigue damage behaviour of the aluminium cast alloy AlSi7Mg0.3. Materials Science and Engineering: A, 2013, 565: 21-26. https://doi.org/10.1016/j.msea.2012.12.047.

[56] AMMAR, H. R.; SAMUEL, A. M.; SAMUEL, F. H. Effect of casting imperfections on the fatigue life of 319-F and A356-T6 Al–Si casting alloys. Materials Science and Engineering: A, 2008, 473(1-2): 65-75. https://doi.org/10.1016/j.msea.2007.03.112.

[57] BUFFIERE, J.-Y.; SAVELLI, S.; JOUNEAU, P. H.; MAIRE, E.; FOUGÈRES, R. Experimental study of porosity and its relation to fatigue mechanisms of model Al–Si7–Mg0. 3 cast Al alloys. Materials Science and Engineering: A, 2001, 316(1-2): 115-126. https://doi.org/10.1016/S0921-5093(01)01225-4.

[58] WANG, Q. G.; APELIAN, D.; LADOS, D. A. Fatigue behavior of A356/357 aluminum cast alloys. Part II–Effect of microstructural constituents. Journal of light metals, 2001, 1(1): 85-97. https://doi.org/10.1016/S1471-5317(00)00009-2.

[59] FISCHER, C.; SCHWEIZER, C. Experimental investigation of the damage characteristics of two cast aluminium alloys: Part III–Influence of the local microstructure and initial defect size on the fatigue properties. International Journal of Fatigue, 2021, 152: 106388. https://doi.org/10.1016/j.ijfatigue.2021.106388.

[60] GALL, K.; YANG, N.; HORSTEMEYER, M.; MCDOWELL, D. L.; FAN, J. The influence of modified intermetallics and Si particles on fatigue crack paths in a cast A356 Al alloy. Fatigue and Fracture of Engineering Materials and Structures, 2000, 23(2): 159-172. https://doi.org/10.1046/j.1460-2695.2000.00239.x.

[61] FAN, K. L.; HE, G. Q.; LIU, X. S.; LIU, B.; SHE, M.; YUAN, Y. L.; YANG, Y.; LU, Q. Tensile and fatigue properties of gravity casting aluminum alloys for engine cylinder heads. Materials Science and Engineering: A, 2013, 586: 78-85. https://doi.org/10.1016/j.msea.2013.08.016.

[62] HASKEL, T.; VERRAN, G.O.; BARBIERI, R. Rotating and bending fatigue behavior of A356 aluminum alloy: Effects of strontium addition and T6 heat treatment. International Journal of Fatigue, 2018, 114: 1-10. https://doi.org/10.1016/j.ijfatigue.2018.04.012.

[63] REN, P.-R.; SONG, W., ZHONG, G.; HUANG, W.-Q.; ZUO, Z.-X.; ZHAO, C.-Z.; YAN, K.-J. High-cycle fatigue failure analysis of cast Al-Si alloy engine cylinder head. Engineering Failure Analysis, 2021, 127: 105546. https://doi.org/10.1016/j.engfailanal.2021.105546.